

Non-Born–Oppenheimer wavepacket dynamics in polyatomic molecules: vibrations at conical intersections in DABCO†

Andrey E. Boguslavskiy,^a Michael S. Schuurman,^a Dave Townsend^b and Albert Stolow^{*a}

Received 23rd December 2010, Accepted 8th February 2011

DOI: 10.1039/c0fd00033g

The role of vibrational dynamics in the vicinity of conical intersections is investigated using the first two electronically excited states of 1,4-diazabicyclo[2,2,2]octane (DABCO) by combining time-resolved photoelectron spectroscopy with *ab initio* computation. Upon resonant excitation of the origin band of the short-lived S_2 ($^1E'$) state, oscillations in the electronic population between the S_2 ($^1E'$) and the S_1 ($^1A_1'$) electronic states are observed with a period of ~ 3 ps. *Ab initio* computations are employed to characterise these low-lying excited states, which arise from single excitations into the 3s and 3p Rydberg orbitals. Although Rydberg states are generally only weakly coupled, DABCO exhibits rapid nonadiabatic dynamics. This implies that strong coupling occurs only in the immediate vicinity of a conical intersection, enabling unique identification of those vibrations which generate the nonadiabatic transitions. To this end, seams of conical intersection are located at energetically relevant geometries, engendered by differential distortions of the S_1 and S_2 potentials due to vibronic coupling and a Jahn–Teller-distorted S_2 minimum energy point. From an analysis of the conical intersection topography, those vibrations leading to a maximal modulation of the coupling between the electronic states are readily identified. The observed oscillation in the decay of S_2 state population is thereby assigned to the beat frequency between two sets of vibronic eigenstates within the S_1 manifold, coherently prepared together with another set at the S_2 band origin, and whose nominal e' degeneracy is lifted due to differential coupling to the Jahn–Teller-distorted components of S_2 .

1. Introduction

Dynamics in the excited states of polyatomic molecules are generally more complicated than those in the ground state because of the breakdown of the Born–Oppenheimer approximation (BOA). This occurs when the parametric dependence of electronic energy on nuclear coordinates, implicit in the adiabatic approximation, becomes a functional one and typically manifests when electronic states come into close energetic proximity. This situation brings about an associated increase in the

^aSteeacie Institute for Molecular Sciences, National Research Council of Canada, 100 Sussex Dr., Ottawa, Canada K1A 0R6

^bSchool of Engineering & Physical Sciences, Heriot-Watt University, Edinburgh, EH14 4AS, UK

† Electronic supplementary information (ESI) available: Tables containing calculated harmonic frequencies in ground and excited state minima as well as geometries of all pertinent energy minima and minimum energy conical intersections (MECI). See DOI: 10.1039/c0fd00033g

derivative coupling, due to the nuclear kinetic operator, between the now near-degenerate electronic states. A particularly relevant breakdown of the BOA occurs when two (or more) electronic states are degenerate at a specific nuclear configuration. If the degeneracy of the electronic states in the vicinity of this point is lifted linearly upon nuclear displacement, it is termed a conical intersection (CI). Far from being mere isolated points, CIs form $(N_{\text{vib}} - 2)$ -dimensional seams along which the two electronic states are degenerate. In the two coordinates that lift the degeneracy, the potential energy surfaces resemble a double cone with the CI at the apex. Nuclear displacements along these two coordinates span the so-called **g-h** plane,^{1,2} where the vector **g** is defined as the energy difference gradient between the two states, and the vector **h** is collinear with the nonadiabatic coupling gradient. Passage through a conical intersection generally results in ‘radiationless transition’ from one electronic state to another and is effectively described by a small subset of vibrational modes/internal coordinates. Conical intersections are extremely efficient at facilitating these transitions and can lead to femtosecond timescale nonadiabatic dynamics.

Intuition suggests that there should be correlations between intersection topography and the efficiency of the corresponding nonadiabatic transition. If the cone axis is vertical, the orientation of approach to the coupling region is not of particular import in determining the probability of a nonadiabatic transition to a different adiabatic state (although it may be very important in determining the nature of the final state). This yields the canonical picture of a photochemical funnel, wherein upper state population is very efficiently directed through the apex of the cone, particularly if the crossing is in the vicinity of a potential minimum. In this case, the gradients of the potential energy surface direct a wavepacket to the coupling region. If the cone axis is significantly tilted, the direction of approach may have a profound impact on the probability of a nonadiabatic transition occurring. Some trajectories may pass efficiently through these sloped CIs, whereas others may not. In fact, recrossing of the conical intersection is a possible outcome in this situation. It might be said that conical intersections play a role in excited state dynamics analogous to that of the transition state in ground state reaction dynamics. In the latter case, the Polanyi rules relate the topographical feature of the transition state and associated vibrational dynamics to the outcomes and energy disposal of the reaction. By analogy, therefore, we might expect that specific vibrational motions at CIs will be as important to the dynamics as are the topographical features of the CI itself. Exploring the role of vibrational dynamics at CIs is the focus of the present investigation.

Using an approach based upon the systematic substitution of H atoms with methyl groups, we have begun to explore vibrational dynamics at CIs, with relevant examples being the unsaturated hydrocarbons³⁻⁵ and the α,β -enones.⁶ In general, the experimental study of vibrational dynamics at CIs is challenged by the extreme rapidity of the nonadiabatic dynamics. Furthermore, strong coupling generally creates a large CI ‘‘volume’’, the regions of configuration space over which the nonadiabatic coupling is large. Recent quantum dynamical simulations⁷ have shown that in the case of the strongly coupled S_0 and S_1 states in ethylene, efficient population transfer is observed even when the energy gap between the states is greater than 0.5 eV. Strong coupling leads to a ‘‘delocalisation’’ of the effects of the CI and tends to therefore obscure the analysis of specific vibrational motions at CIs. In order to further our understanding and to assist in the development of heuristic pictures of such dynamics, it will be helpful to find limiting case systems which experimentally exhibit vibrational dynamics between electronic states that are weakly coupled (slower time scales), with configurationally highly localised CI volumes, which therefore show sensitivity to specific vibrational motions. This situation corresponds to the sparse coupling limit of the radiationless transition problem, as opposed to the well known statistical (*e.g.* Bixon–Jortner) limit where the density of nonadiabatically coupled states form an ‘apparent’ quasi-continuum, leading to

'exponential decay' of the optically prepared state. In the sparse coupling limit, we expect enhanced sensitivity of the nonadiabatic dynamics to specific vibrational motions. With respect to identifying limiting case paradigms, we suggest that CIs between Rydberg states of high symmetry polyatomics will be a useful avenue for this exploration. Specifically, we investigate here, by combining femtosecond time-resolved photoelectron spectroscopy with *ab initio* computation, the vibrational dynamics at CIs in the Rydberg S_2 electronic state of 1,4-diazabicyclo[2,2,2]octane (DABCO), whose structure is shown in Fig. 1 (bottom right).

The considerable number of experimental and theoretical investigations into the electronic structure of DABCO gives some indication of the level of interest this molecule has elicited. Much of this attention stems from the fact that DABCO is a paradigmatic example of an alkylamine: a group of molecules whose electronic structure is closely related to that of ammonia, undergoing significant geometric relaxation upon electronic excitation.⁸ Initial experimental studies on the low-lying electronic states of DABCO employed absorption spectroscopy.⁸ While the electronic character of the observed bands was not assigned, the first strong band was identified as a $p \leftarrow N$ type transition. While subsequent spectroscopic investigations employed UV absorption and emission spectroscopy,^{9,10} the nature of these states wasn't firmly established until 2-photon REMPI and LIF experiments¹¹ identified the first excited state as a $3s(1A_1') \leftarrow N$ transition (forbidden for one-photon processes) at 4.44 eV, and the first optically bright state, observed at 4.94 eV, was assigned to the $3p_{xy}(1E') \leftarrow N$ transition. A comparison of the first two ionisation potentials, in conjunction with *ab initio* computations,^{12,13}

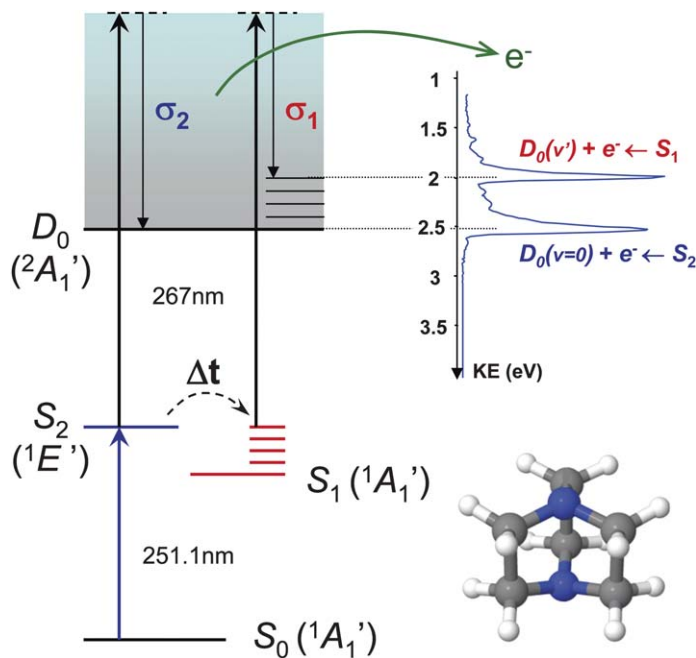


Fig. 1 DABCO, shown bottom right, is studied *via* fs time-resolved photoelectron spectroscopy. The doubly degenerate S_2 and the non-degenerate S_1 states each have Rydberg character and each correlate upon ionisation to the D_0 cation ground state. Jet-cooled molecules are resonantly pumped to the S_2 vibronic origin by a 251.1 nm pump pulse, and subsequently ionised by a time-delayed 267 nm probe pulse. The electronic states are labelled employing D_{3h} symmetry. Nonadiabatic coupling causes the initially prepared vibrationless S_2 state to evolve into a vibrationally excited S_1 state. Emitted photoelectrons are energy resolved at each time delay in order to generate the time-resolved photoelectron spectrum.

determined that the HOMO orbital in DABCO is the $p_z(+)$: the symmetric combination of the p_z orbitals on the bridging nitrogen atoms that, perhaps surprisingly, lies above the $p_z(-)$ combination which displays a node between the two nitrogens.

Computational studies of the character of the excited state manifold have been relatively successful in reproducing these experimental observations. A systematic study of a series of caged alkylamine species, employing HF/6-31G* optimised ground state structures and DZ/SAC-CI energies, computed the $3s$ ($^1A'_1$) and $3p_{xy}$ ($^1E'$) states to lie at 4.53 eV and 4.98 eV, in reasonable agreement with experiment.¹⁴ Additionally, a third, low-lying $^1A''_2$ excited state was predicted at 5.05 eV. Denoted $3p_z$ in that report, this state is the $3s(-)$, and was computed to have an oscillator strength approximately 1/250 that of the $^1E'$ state. The molecular orbitals of DABCO obtained from our calculations (*vide infra*) are shown in Fig. 2. As discussed in more detail below, the S_1 and S_2 excited states arise from single excitations into the $3s(+)$ and $3p_{xy}(+)$ orbitals, respectively. Coincidentally, observation of the $3p_z(-)$ has been reported in a magnetic circular dichroism study¹⁵ at an energy of 6.29 eV, much further into the UV than may have been expected. Given the width of the $^1E'$ state absorption band, direct experimental observation of the $3s(-)$ has been challenging. An initial assignment of the $^1A''_2$ band origin in a laser ionisation study¹⁶ was later assigned to autoionising Rydberg states accessed *via* an excited S_1 vibrational state.¹⁷

It might be expected that a spectroscopic determination of the $3s(-)$ state could be achieved *via* the extrapolation of a corresponding Rydberg series. To this end, extrapolation of the $n = 12$ –41 Rydberg series, tentatively assigned to the $ns(-)$ series and measured by 2-colour multiphoton absorption spectroscopy,¹⁸ predicts the $3s(-)$ ($^1A''_2$) band origin to be located at 4.0 eV. This value is severely red-shifted relative to all existing computations. Similar extrapolations can be performed using Rydberg series measured using fluorescence dip¹⁹ and ZEKE spectroscopy,²⁰ each yielding lower than expected values, relative to computation, for the $3s(-)$ band origin. Such Rydberg extrapolations, however, would be expected to be somewhat unreliable since the orbital radius of the $n = 3$ Rydberg electron is $\sim n^2 \approx 9a_0$, a value small enough to be comparable in size to the nuclear framework of the molecule. Thus, the low-lying Rydberg states in the series would be significantly more perturbed by the core than those at large values of n .

The structural aspects of DABCO have also been extensively studied, beginning with an early electron gas diffraction²¹ study that reported the ground state of DABCO was slightly twisted about the C_3 rotational axis, giving rise to a D_3 symmetry minimum energy structure. The small potential maximum at the D_{3h} saddle point was estimated to be only 35 cm^{-1} above the D_3 minima, whereby the structure of the minimum was denoted “quasi- D_{3h} ”. Numerous subsequent studies have examined this particular aspect of the vibrational spectrum. Multiphoton ionisation studies¹³ concluded that the torsional potential in the S_1 state was stiffer than that in the S_0 state, resulting in a ‘more D_{3h} ’ structure. This analysis was in agreement with later REMPI,²² MPI-optogalvanic spectroscopy,²³ and LIF²⁴ studies. Spectroscopic results for these torsional frequencies have largely converged on values of $\nu \approx 60 \text{ cm}^{-1}$ for the ground state, and $\nu \approx 100 \text{ cm}^{-1}$ for the S_1 torsional frequency.

The nominally E' symmetry S_2 state is subject to Jahn–Teller distortions and will thus display energy minima of lower point group symmetry. While no detailed spectroscopic studies on the vibrational structure of the $n = 3$ $^1E'$ state have been performed to date, fluorescence dip spectroscopy¹⁹ was employed to observe the splitting of the e' symmetry vibrational modes of the $n = 4$ p_{xy} (E') state. It was found that all the observed e' modes were split, leading to the inference that the Jahn–Teller coordinate was a complex mixture of a number of vibrational modes. As predicted by theory,²⁵ the magnitude of the Jahn–Teller splitting decreased with increasing principle quantum number n .

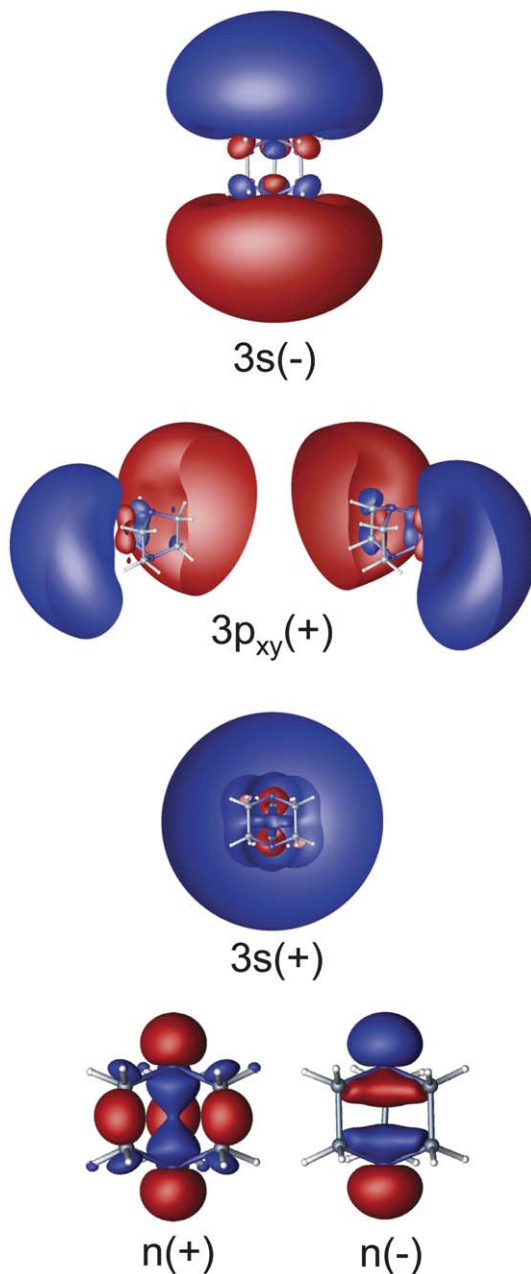


Fig. 2 Molecular orbitals of DABCO. The highest occupied molecular orbital (HOMO) is denoted $n(+)$ and arises from the 'plus' combination of the $N p_z$ orbitals, while the 'minus' combination yields the HOMO-1 [$n(-)$] orbital. The lowest lying excited states, denoted S_1 , S_2 , and S_3 in the text, arise from single excitations into the $3s(+)$ and $3p_{xy}(+)$ (which together transform as e') and $3s(-)$ orbitals, respectively.

In this report, time-resolved photoelectron spectroscopy (TRPES)^{26,27} is employed to probe the behaviour of non-Born–Oppenheimer wavepackets prepared by photoexcitation to the band origin of the S_2 electronic state. Interesting time dependent behaviour in DABCO was noted in previous TRPES studies:²⁸ the decay of the S_2

photoelectron signal was observed to display a modulation. However, it was not possible at that time to associate the modulated S_2 signal with any corresponding dynamics in the S_1 state. More recently, a time-resolved study of the vibrational dynamics within the S_1 manifold reported oscillatory behaviour that was explained as an interference effect between two S_1 vibrational fundamentals.²⁹

Although wavepackets can classically localise certain degrees of freedom, yielding an intuitive picture of the dynamics, they also exhibit non-classical behaviour such as dephasing and revival. Both revivals and fractional revivals have been observed in molecular vibrational wavepackets. Femtosecond pump–probe studies on NaI and NaBr by the Zewail group^{30–32} revealed oscillations between ionic and covalent dissociation channels that were accessed upon photoexcitation. The 1.25 ps period of oscillation for the NaI experiment corresponds to a level splitting of $\sim 27\text{ cm}^{-1}$, which was in agreement with the level spacing between the two states. Similar experiments, in which oscillations between exit channels of a photodissociation process, were also observed in IBr.^{33,34} Oscillations between two bound states have been observed in Rb_2 for the coupled $A\ ^1\Sigma_u^+$ and $b\ ^3\Pi_u$ electronic states.³⁵ In polyatomic molecules, however, such non-Born–Oppenheimer revivals are presumed to be exceedingly uncommon given the rate and efficiency of intramolecular vibrational energy redistribution (IVR) processes.

In the following, we present our time domain studies of a non-Born–Oppenheimer wavepacket in the polyatomic molecule DABCO, initially prepared at its S_2 band origin and probed using TRPES. The important regions of the potential energy surfaces of the pertinent excited electronic states were elucidated using high level *ab initio* electronic structure computations. In Section 2, we outline the details of the methods employed, both experimental and theoretical. In Section 3, we present the results of the spectroscopic studies and computations, while in Section 4 we discuss and interpret these findings. In Section 5, we summarise and conclude this report and indicate avenues for further investigation.

2. Methods

2.1 Experimental methods

TRPES experiments were performed using a magnetic bottle photoelectron spectrometer^{36,37} employing a seeded, pulsed supersonic molecular beam. The beam was produced by a 1 kHz EL (Even–Lavie) pulsed valve. DABCO crystals heated to $\sim 80\text{ }^\circ\text{C}$ in the sample cartridge and seeded in helium at a stagnation pressure of 15 kTorr were expanded through a conical nozzle 250 μm in diameter to generate a pulsed molecular beam. The beam was skimmed and introduced into the ionisation chamber where the background pressure during the experiment was *ca.* 10^{-8} Torr (base pressure *ca.* 2×10^{-9} Torr).

The photoelectrons produced by the ionisation process are born at the focus of the magnetic bottle (1 T). Electrons were guided towards the triple stack microchannel plate detector by a weak (10 G) constant homogeneous magnetic field. The photoelectron time-of-flight depends on electron energy but, because of rapid parallelisation of trajectories, it is almost independent of the initial direction of emission. A 1 V retarding potential was applied to a transmission mesh in order to slow down the generated photoelectrons, thereby achieving better energy resolution. The components of the terrestrial magnetic field perpendicular to the flight tube were compensated by two sets of Helmholtz coils. The detector was operated in the single electron (event counting) mode. Data was collected at the rate of a few counts per laser shot to ensure that signals generated were linear in both pump and probe laser pulse energies (*i.e.* avoiding multiphoton processes).

Femtosecond laser pulses were generated by frequency mixing of the output of a 1 kHz Ti:Sa regenerative amplifier (Coherent Legend). A portion of the 800 nm pulse was converted to the third harmonic (0.5 μJ) and used as the probe. The

pump beam (0.2 μJ) at $\lambda = 251$ nm was obtained by mixing the second harmonic of an optical parametric amplifier (TOPAS) with the Ti:Sa fundamental, followed by subsequent second harmonic generation. Group velocity dispersion and pre-compensation was managed in each beam by a pair of VUV grade CaF_2 prisms. The pump and probe pulses were combined collinearly at a dichroic mirror and loosely focused ($f/250$) into the spectrometer using spherical reflective optics. The focal volume averaged laser intensities were estimated to be 5×10^9 and 3×10^{10} W cm^{-2} for pump and probe pulses, respectively. The pump pulse polarisation was orthogonal to the time-of-flight axis of the spectrometer. A $\lambda/2$ waveplate in the 267 nm (probe) beam was used to control the relative polarisation state of the probe laser. The time resolution (cross correlation) was determined by measuring the non-resonant $[1 + 1']$ photoionisation of nitric oxide seeded in a molecular beam. A set of peaks arising from the ionisation of nitric oxide by $[2 + 0]$, $[1 + 1']$, $[0 + 2']$, and $[1 + 2']$ processes (under increased laser intensities) were used for energy calibration of the photoelectron spectrometer. The spectral bandwidths of the pump and probe pulses were ~ 200 cm^{-1} .

The probe beam was optically delayed with respect to the pump beam using a hollow corner cube retroreflector on a computer controlled delay stage. At each time delay a sequence of accumulating photoelectron counts due to pump + probe, pump only, and probe only were collected, the latter two being used for dynamic background subtraction.

A schematic of the pertinent vibronic energy levels involved in the time-resolved photoelectron spectroscopy experiment are indicated in Fig. 1. DABCO molecules are resonantly promoted into the S_2 vibronic origin band at 251.1 nm and subsequently ionised with a time-delayed 267 nm laser beam. Emitted photoelectrons were detected and energy resolved at each pump–probe delay in order to generate a time-resolved photoelectron spectrum.

2.2 Theoretical methods

All optimised minima and minimum energy conical intersections (MECI) were determined employing *ab initio* electronic structure methods. The electronic wavefunctions were computed at the multireference configuration interaction singles and doubles (MR-CISD) level of theory using Dunning polarised double- ζ basis functions, where a diffuse 3s ($\zeta = 0.028$ and 0.023 for C and N, respectively) and 3p ($\zeta = 0.025$ and 0.021 for C and N, respectively) set of functions were employed on the C and N atoms,^{38–41} while a Dunning DZ basis set^{38–41} was used for the H atoms, a basis that is cumulatively denoted ‘DZP+’ in the following discussion. The active space for the generation of the CASSCF reference functions included the HOMO (a'_1) and HOMO-1 (a''_2) orbitals in addition to the 3s and 3p_x, 3p_y, and 3p_z Rydberg orbitals (Fig. 2). The conical intersections, including the minimum energy D_{3h} Jahn–Teller point, were optimized employing a Lagrange multiplier constrained optimisation approach,⁴² using analytic energy^{43,44} and nonadiabatic coupling gradients.^{45,46} The curvature of the potential energy surface at all stationary points was characterised by the determination of the Hessian and corresponding harmonic vibrational frequencies. The force constant matrices were determined *via* the computation of analytic gradients at geometries displaced along internal coordinates. All electronic structure computations were performed using the COLUMBUS suite of programs.^{47,48}

3. Results

3.1 Experimental results

3.1.1 Time-resolved photoelectron spectra. In Fig. 1 we present the time integrated photoelectron spectrum of DABCO excited to the origin band of the $S_2(^1E')$ transition, which shows two sharp photoelectron bands originating from

ionisation of S_2 at higher kinetic energy (near 2.5 eV) and S_1 at lower kinetic energy (just below 2.0 eV). The sharp, single-featured photoelectron spectra for both the S_2 and the optically dark S_1 state are consistent with the known Rydberg character of these two states. Furthermore, the absence of Franck–Condon progressions suggests that the differences between the excited-state and cationic geometries are relatively small, implying that both sets of Rydberg states converge to the same cationic state (D_0). Since the dynamical processes take place in a collisionless molecular beam, the total energy within each molecule is conserved. Thus, as the non-Born–Oppenheimer wavepacket evolves, the total energy of the system (defined by the energy of the pump laser photon) remains constant, implying a time-dependent conversion (from S_2 to S_1) of electronic to vibrational energy.

Due to the propensity for Rydberg states to favour Franck–Condon diagonal ($\Delta v = 0$) transitions, photoionisation of the vibrationally cold S_2 state produces the vibrationless cation D_0 ground state (Fig. 1). Similarly, photoionisation of vibrationally hot S_1 state produces vibrationally hot levels in D_0 . Therefore, the time evolution of the electronic character of this non-Born–Oppenheimer wavepacket may be viewed quite transparently in the full 2D time- and energy-resolved TRPES spectrum (Fig. 3a). The energy difference observed between the S_1 and S_2 photoelectron peaks is ~ 0.5 eV, in good agreement with both frequency domain spectroscopy,^{8,11,16} where two-photon spectroscopy permits the direct observation of both the S_1 and S_2 origins, and with previous *ab initio* computations.¹⁴

The channel-resolved photoelectron yields, each energy integrated within the band bounded by the dashed lines, are plotted as a function of time in Fig. 3b, showing an apparent counter-phased oscillation in photoelectron yield between the S_2 and S_1 bands. The use of photoelectron spectroscopy as the probe permits the simultaneous monitoring of both states and suggests that this oscillation occurs specifically as a result of population transfer between the S_2 and S_1 electronic states, and is not due to vibrational coupling within the same electronic state. The simultaneous fit to both traces with an exponential kinetic model, convoluted with a cosine oscillatory component and the Gaussian cross-correlation response, yields an adequate first order description. With this we obtained a S_2 lifetime of $\tau \approx 3$ ps and an oscillation frequency of $\omega = 11$ cm^{-1} , as shown in Fig. 3b. However, further examination of the data revealed the apparent presence of multiple oscillatory components. This analysis depended on disentangling the statistical (*i.e.* exponential decay) behaviour from the experimental data. This was accomplished *via* 2D global Levenberg–Marquardt fitting of the photoelectron spectra, simultaneously at all time delays and photoelectron kinetic energies, to a sequential kinetic model. While the simplest sequential kinetic model $S_2 \rightarrow S_1 \rightarrow S_0$ reasonably reproduces the behavior of the non-oscillatory dynamics, we found that better global agreement is reached when the data is fit to a sum of two exponential functions. The forms of the decay-associated spectra (*i.e.* the amplitudes of these two exponential components as a function of photoelectron kinetic energy) are similar, suggesting that the need for a second exponential function arises from a non-exponential kinetic process, rather than a contribution from some other electronic state.

The mere presence of an oscillatory component in the time-resolved spectrum indicates we are in a non-statistical/sparse coupling regime. Therefore, there is no *a priori* justification for mono-exponential decay of the photoelectron spectra. In this sense, it is unremarkable that two exponents naturally yield a better fit. Secondly, the preponderance of the measurements were performed with parallel pump and probe laser beam polarisations. In DABCO, the timescales for rotation ($T_{\text{avg}} \sim 1/cE_{\text{avg}} = h/kT_{\text{rot}} = 1.6$ ps for $T_{\text{rot}} = 30$ K) and $S_2 \rightarrow S_1$ conversion are on similar time scales. In this situation, the Gaussian-like time dependence of the initial stage of rotational dephasing^{49–51} will factorise with the true intramolecular decay. This may alter the time constants, but should not have much affect on the oscillatory component of the dynamics which is the primary concern of this report. In order to proceed further, we subtracted the 2D Levenberg–Marquardt

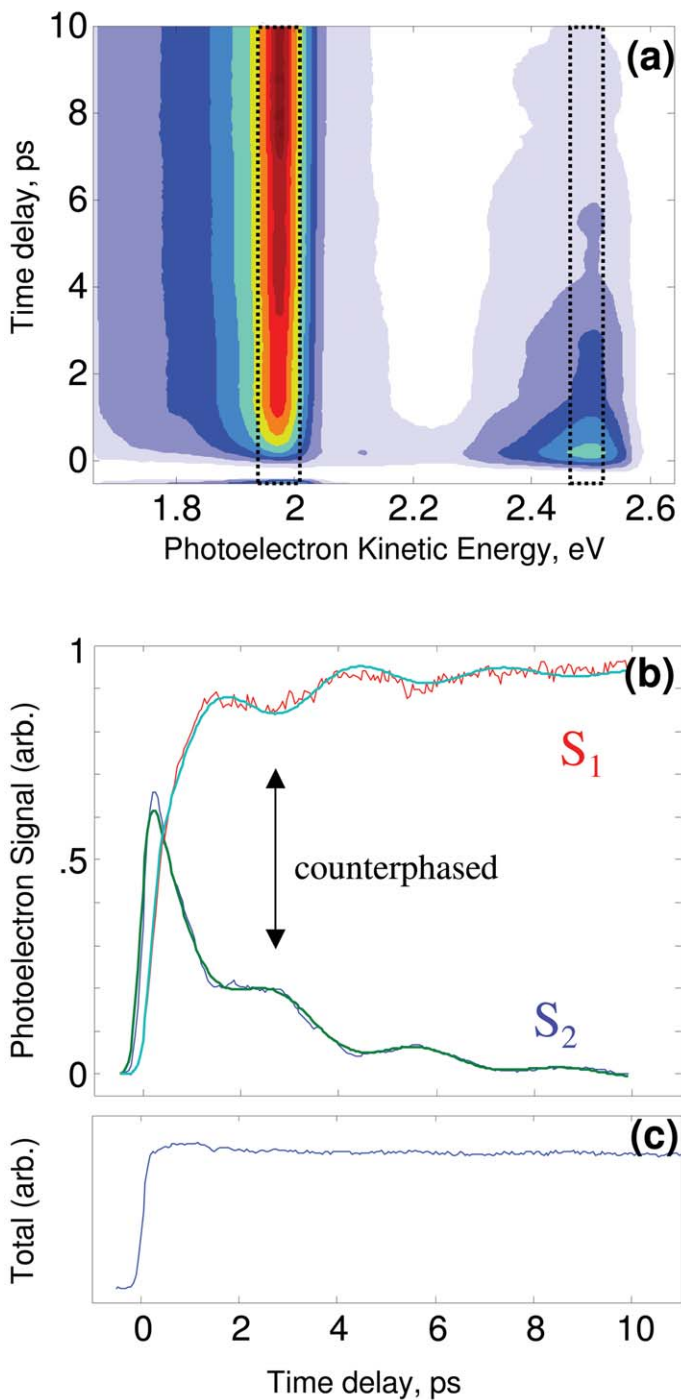


Fig. 3 (a) Time resolved photoelectron spectrum of DABCO following excitation to the S_2 origin band at $\lambda = 251.1$ nm, and subsequent ionisation into D_0 with a time delayed 267 nm laser pulse. Photoionisation of the initial vibrationless S_2 state produces the photoelectron band near a kinetic energy of 2.5 eV. Due to nonadiabatic coupling, this band decays as a function of time, transforming into a lower energy band near 1.95 eV kinetic energy due to

biexponential fit from the 2D data for Fig. 3a, leaving as residual the purely oscillatory component, shown in Fig. 4a. The counterphased oscillations are clearly seen. The residuals were subsequently analysed *via* Fourier transformation. The Fourier power spectra presented in Fig. 4b clearly show the fundamental 11 cm^{-1} beat as well as some higher frequency components. The presence of multiple frequencies in the Fourier power spectra likely indicates that vibrational energy liberated upon $S_2 \rightarrow S_1$ internal conversion flows into vibronic energy levels characterised by more than one vibrational mode.

3.1.2 Rotational and vibrational cooling. In order to assess the effect of jet cooling on the modulation depth of the oscillations, the experiment was repeated under different molecular beam expansion conditions. It was determined that a continuous molecular beam expansion through a $50\text{ }\mu\text{m}$ pinhole and 1.8 bar of backing pressure leads to a reduction in contrast to the point that the oscillations are practically unobservable. It was only after extensive data averaging that traces of the revivals could be detected. Upon expansion with 20 bar backing pressure, there was a pronounced increase in the modulation depth of the oscillations. While it is not expected that there will be significant cooling of most vibrations in a supersonic gas expansion, the very low-frequency torsional vibrations in DABCO are likely to be cooled quite efficiently.

Since the rotational constants of DABCO are $\sim 0.02\text{ cm}^{-1}$, even at rotational temperatures as low as a few degrees Kelvin, one cannot completely avoid rotational averaging. On the other hand, with the linearly polarised pump and probe pulses set at a magic angle configuration, the molecular rotations do not directly influence the observation of non-Born–Oppenheimer wavepacket dynamics. Only *via* a second-order perturbation, such as an additional centrifugal term in the potential energy curves or Coriolis coupling between vibrations and rotations, would rotations remain of concern with a magic angle geometry. In a warm sample, the numerous hot bands would lead to an incoherent sum of initial wavepackets propagating on slightly different regions of the molecular potential, thus reducing the contrast of the electronic revivals.

The lowest frequency vibration in DABCO corresponds to a torsional mode (a''_1) about the C_3 axis. Using electron diffraction measurements, a value of 29 cm^{-1} (ref. 21) was determined for the S_0 electronic state fundamental. This mode is manifested through a sequence bands in the $S_1 \leftarrow S_0$ multiphoton ionisation spectrum as 54 cm^{-1} ,²² $125/2\text{ cm}^{-1}$.²³ Excitation of this mode *via* a dipole transition is symmetry forbidden (although excitation of an even number of quanta is possible, the corresponding peaks were not observed in the S_2 absorption spectrum^{8,10,16}). We note, however, that there will be population of this low frequency mode in a Boltzmann ensemble at $T \sim 300\text{--}400\text{ K}$. As will be seen in the next section, the S_1 electronic state in DABCO is also slightly twisted around the N–N axis, whereas the S_2 state is not. This suggests the nonadiabatic transitions between the two states will likely be sensitive to the degree of the twist excitation. Again, we expect that population of vibrational hot bands would further reduce the contrast of the revivals.

photoionisation of the vibrationally excited S_1 state. (b) Channel-resolved photoelectron yield as a function of time, obtained by integration over the energy slices corresponding to the S_2 (dashed lines around 2.5 eV) and S_1 (dashed lines around 1.95 eV) photoionisation bands. Simultaneous fit to both the S_2 and S_1 time traces using a cosine-modulated bi-exponential function [$\text{Signal}(t) = A_1 + A_2\exp(-t/\tau_1) + A_3\exp(-t/\tau_2)\cos(\omega t + \phi)$ where $\tau_1 = 1\text{--}1.3\text{ ps}$, $\tau_2 = 3\text{--}5\text{ ps}$, $\omega = 2h \cdot 3\text{ ps} (= 11\text{ cm}^{-1})$] are superimposed on the experimental data. The clear counterphasing of the S_2 and S_1 photoelectron yields show that the zeroth-order electronic population is directly modulated by vibrational motion. (c) The total energy-integrated photoelectron yield as a function of time. This demonstrates that the $S_2(v=0)$ and $S_1(v=v')$ photoionisation cross-sections are essentially the same and that there are no other intervening dark states.

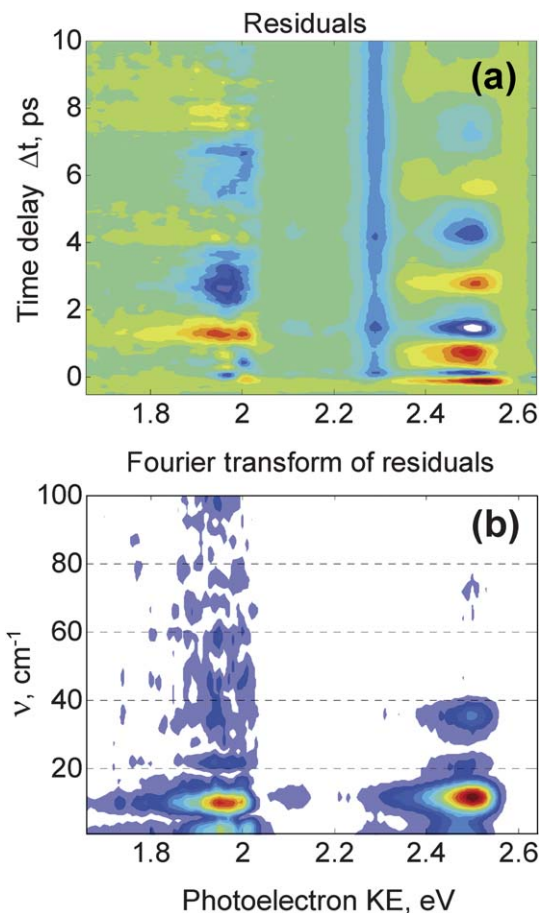


Fig. 4 (a) Deconvolution of the decaying components of the DABCO TRPES spectrum leaves a residual which shows the oscillatory behaviour of the zeroth-order electronic population. (b) The Fourier power spectrum of the oscillatory residual from (a) reveals a very strong modulation at 11.5 cm^{-1} . Along the S_2 band (near 2.5 eV), higher frequency modulations are seen, but only weakly, at 21 , 35.5 , and 72 cm^{-1} . Along the S_1 band (near 1.95 eV), a broader set of higher frequencies is seen, also weakly.

3.2 Computational results

The ground electronic state of DABCO is a closed-shell singlet in which the highest occupied molecular orbital (a'_1 , HOMO) is the in-phase combination of the p_z -orbitals on the bridging N atoms, while the HOMO-1 (a''_2) orbital is the out-of-phase combination. The lowest-lying excited states arise from excitations out of the HOMO into the $n = 3$ manifold of Rydberg orbitals. Density plots of these orbitals are rendered pictorially in Fig. 2. The global minimum on the ground state surface is distorted from D_{3h} symmetry by a 9° twist about the C_3 axis, yielding a minimum energy structure with D_3 symmetry. However, the barrier to rotation about the C_3 axis is exceedingly small, computed at the present level of theory to be 20 cm^{-1} , in agreement with previous experimental results that determined the ground electronic state to be quasi- D_{3h} .²¹ A subset of pertinent geometric parameters for the ground state minimum energy structure, as well as minimum energy points on the excited state surfaces, are presented in Table 1. A complete specification of the molecular geometry at each point is given, in Cartesian geometries, in Tables S2–S8.†

Since the HOMO orbital gives rise to a bonding interaction between the bridging N atoms, excitations out of this orbital have a significant impact on the N–N distance, which is uniformly larger for the excited state minima. Likewise, while the ground state umbrella modes are symmetric and anti-symmetric combinations of vibrations at each N atom (634 cm⁻¹ and 829 cm⁻¹, respectively), these modes are largely uncoupled on the excited state surfaces. The vibrational frequencies at all the stationary points on the ground and excited state surfaces are given as ESI in Table S1.†

The first excited state is optically dark and arises from an excitation into the 3s Rydberg orbital, ostensibly yielding the ¹A₁ state. However, the minimum on this surface is distorted both along the *a*'₁ twist coordinate (by 6.5°) and the *a*'₂ antisymmetric N-pyramidalisation coordinate (Δγ = 3.1°, where γ is the pyramidalisation angle at the bridging N atoms), yielding a minimum energy structure with C₃ point-group symmetry. The resultant adiabatic excitation energy of 4.36 eV, evinced in Table 2, is in good agreement with the experimental value of 4.44 eV.

The bright S₂ state arises from an excitation into the degenerate Rydberg 3p_x and 3p_y, which together form an *e*' molecular orbital, giving rise to a ¹E' state. It is immediately apparent that this open-shell singlet is an (*E*' × *e*') Jahn–Teller system, which will distort to yield three equivalent C_{2v} symmetry minima connected by three equivalent C_{2v} symmetry saddle points. In this case, the magnitude of the distortion is quite small, with the lower ¹A₁ state stabilised by only 7 cm⁻¹ from the Jahn–Teller point. Unsurprisingly, this corresponds to relatively minute geometric distortions such that the differences between the symmetry distinct *r*_{CN} and θ_{CNC} valence internal coordinates are only 0.0008 Å and 0.30°, respectively, while the difference between the *r*_{CC} are <10⁻⁴. The computed adiabatic excitation energy of 4.74 eV is somewhat lower than the spectroscopically determined value of 4.94 eV.

The last state considered in this study involves excitation to an *a*'₂ symmetry Rydberg orbital comprised of the minus combination of the diffuse 3s functions on each of the N atoms, denoted 3s(–) here as well as in previous studies.^{13,17} The minimum energy point on this surface retains D_{3h} symmetry and displays a moderate geometric relaxation of 0.35 eV to the minimum energy structure, giving rise to adiabatic excitation energy of 4.79 eV. This value is somewhat lower than that value of 5.06 eV computed in previous computational studies.¹⁴

When considering nonadiabatic transitions between these low-lying excited states, one would perhaps not initially expect conical intersections to be of particular import. Specifically, since all the states involved are of Rydberg character, it would be reasonable to assume that the potential curves for each of the excited states in the manifold would be nearly parallel, since each converges to the same cationic core. In this scenario, any curve crossings would be expected to occur at very high energies

Table 1 Geometric parameters for minimum energy structures, (Å, degrees)

	<i>R</i> _{min} [S ₀]	<i>R</i> _{min} [S ₁]	<i>R</i> _{min} [S _{2x}]	<i>R</i> _{MECI} [S _{2x} , S _{2y}]	<i>R</i> _{MECI} [S ₁ , S _{2x}]	<i>R</i> _{MECI} [S ₁ , S _{2y}]
¹ N ₁ N ₂	2.5585	2.4532	2.4476	2.4477	2.1666	2.1602
¹ N ₁ C ₁₁	1.4610	1.4391	1.4273	1.4278	1.3206	1.3516
¹ N ₂ C ₂₁	1.4610	1.4334	1.4273	1.4278	1.3210	1.3512
¹ N ₁ C ₁₂	1.4610	1.4391	1.4281	1.4278	1.3542	1.3299
¹ N ₂ C ₂₂	1.4610	1.4334	1.4281	1.4278	1.3541	1.3301
¹ C ₁₁ C ₂₁	1.5555	1.6091	1.6229	1.6228	1.6965	1.7222
¹ C ₁₂ C ₂₂	1.5555	1.6091	1.6227	1.6228	1.6974	1.7037
⁰ N ₁ C ₁₁ C ₂₁	110.0	109.1	106.8	106.8	100.2	99.3
⁰ N ₂ C ₂₁ C ₁₁	110.0	104.9	106.8	106.8	100.3	99.3
⁰ N ₁ C ₁₂ C ₂₂	110.0	109.1	106.8	106.8	100.0	99.9
⁰ N ₂ C ₂₂ C ₁₂	110.0	104.9	106.8	106.8	100.0	99.9
¹ N ₁ C ₁₁ C ₂₁ N ₂	9.1	6.5	0.0	0.0	0.0	0.0

Table 2 Excited state energies at optimised geometries. The values in the first row of the table are the vertical excitation energies and are given in eV. The remainder of the energies in the table are in cm^{-1} and are relative to the minimum energy point on the S_1 surface

	S_1	S_{2x}	S_{2y}	S_3
$R_{\min}[S_0]$	4.67	5.07	5.07	5.12
$R_{\min}[S_0]$	2622	5829	5829	6254
$R_{\min}[S_1]$	0	3093	3093	3993
$R_{\min}[S_{2x}]$	119	2879	2910	3455
$R_{\min}[S_3]$	120	2924	2924	3411
$R_{\text{MECI}}[S_{2x}, S_{2y}]$	112	2887	2887	3448
$R_{\text{MECI}}[S_1, S_{2x}]$	25 422	25 422	25 934	27 062
$R_{\text{MECI}}[S_1, S_{2y}]$	26 592	26 993	26 592	28 178

thus to be of negligible importance. This intuitive picture has some merit, and is in fact an accurate assessment of the potential curves along most of the internal coordinates in the molecule. There are, however, coordinates of notable exception. Firstly, the effect of the distortion along the Jahn–Teller coordinate introduces a pseudo-anharmonicity into this potential curve that is absent on the lower S_1 surface. More importantly, vibronic coupling of the S_1 and S_3 states along the anti-symmetric N-pyramidalisation coordinate gives rise to potential energy curves of significantly different curvature (relative to S_2) along this direction, leading to curve crossings at energetically relevant geometries.

The minimum energy conical intersections of C_s symmetry between both components of the Jahn–Teller distorted state and the S_1 state were optimised at the DZP+/MRCI level. The geometric distortions are relatively small, as seen from the changes in the geometric parameters given in Table 1. The relatively small changes in the valence internal coordinate between these intersections and the region of the excited state minima gives evidence to the rigidity of the caged molecular structure. These minimum energy crossings are found to occur 22 543 cm^{-1} above the S_{2x} state minimum, which corresponds to approximately 1/2 of the zero point energy.

4. Discussion

As discussed in Section 3.2, the S_2 and S_1 states are largely nested, parallel potentials which are perturbed only along a specific subset of coordinates. Using the assumption of perfectly nested potentials and modeling the internal conversion process as a proximity effect (*i.e.* the energy gap law), one ends up with >200 ps lifetime for S_2 , which is much longer than the observed lifetime of $\tau \sim 3$ ps. Our calculations show that DABCO in both its S_2 and S_1 states is in fact slightly distorted from D_{3h} . In the S_2 state, DABCO's distortion is governed by the Jahn–Teller (JT) interaction, which formally lowers the point group symmetry to C_{2v} . In the S_1 state, the molecule is twisted and pyramidalised, resulting in C_3 symmetry. Thus, JT, twist and pyramidalisation are the coordinates along which the S_2 and S_1 potentials will have the greatest difference in curvature and, hence, the highest likelihood of energetically low lying crossings. This is confirmed by an analysis of the **g** and **h** vectors, which can be nearly wholly represented in a basis of Jahn–Teller, twist and pyramidalisation motions. The finding of S_2 – S_1 conical intersections below the S_2 zero point energy supports the experimentally observed rapid dephasing of the S_2 into S_1 .

The experimental TRPES data presented in Fig. 3 and Fig. 4 reveal a time domain behaviour containing an apparent exponential decay convoluted with an oscillatory response. As always in isolated systems, this time behaviour reflects the coherent evolution of the local level structure populated by the broad band (fs) pump laser

pulse. This level structure will emerge from the details of the S_2 - S_1 nonadiabatic coupling at the S_2 origin. The reported S_2 absorption spectrum¹⁶ reveals a single peak (2.6 cm^{-1} FWHM) at the electronic origin, with no other significant absorption peaks seen within 30 cm^{-1} . As there are no true continua (*i.e.* no photodissociation) in DABCO at this energy, the apparent exponential decay should be understood as arising from a high density of irregularly spaced exact (*i.e.* non-Born–Oppenheimer, mixed S_2/S_1) molecular eigenstates. The coherent superposition of these would have an exceedingly long Poincare revival time, leading to observation of an ‘apparent’ irreversible decay. That there is an additional oscillatory component further indicates that there must be a non-monotonic energy dependence to the S_2 - S_1 nonadiabatic coupling, leading to a modulation, with a period of around 11 cm^{-1} , in the coupled state density. A cartoon illustrating one situation consistent with this proposal is depicted in Fig. 5. The zeroth-order, uncoupled (Born–Oppenheimer) \tilde{S}_1 (red) and \tilde{S}_2 (black) states are indicated by their superscript tilde. At the vibrationless origin (indicated as $v = 0$) of the zeroth-order \tilde{S}_2 state, there is a near degeneracy with vibrationally excited levels (indicated as v') of the zeroth-order \tilde{S}_1 state. The nonadiabatic coupling of these leads to the mixed character level structure shown. The lower component, labelled in black as S_2 , is composed of a narrow (*i.e.* ~ 2 – 3 cm^{-1}) but dense band of levels of predominantly zeroth-order \tilde{S}_2 character (indicated by the black segment of each state level). This narrow set of states would correspond to the ‘isolated’ electronic origin peak observed in the UV absorption spectrum, as suggested by the origin spectrum shown on the left. The upper component, at least 30 cm^{-1} but less than 200 cm^{-1} higher in energy, of the mixed S_2/S_1 molecular eigenstates is labelled in red as S_1 and is composed of a broader but still dense set of levels. These levels are comprised predominantly of zeroth-order \tilde{S}_1 character, indicated by the red segment of each state level. In this case, however, due to the non-monotonic coupling, the state mixing as a function of energy is not smooth, as indicated by the variation of the length of the red segment within each state level. This variation would lead to a modulation in the density of optically allowed states, indicated by the bimodal ‘upper level spectrum’ seen on the left. Our experimental data would suggest that these upper levels should come in two clumps, separated by a mean spacing of about 11 cm^{-1} , as shown. In our TRPES experiment,

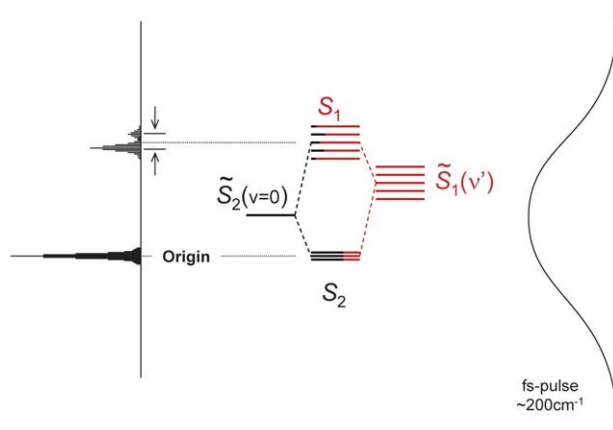


Fig. 5 A proposed DABCO level scheme which is consistent with the TRPES data. The zeroth-order states $\tilde{S}_2(v = 0)$ (black) and $\tilde{S}_1(v')$ (red) nonadiabatically couple to split into the two groups labelled S_2 and S_1 , each of which contains admixtures (red and black) of the zeroth-order electronic state characters. A non-monotonic variation in coupling could lead to a modulation of the level structure as shown in the ‘spectrum’ on the left hand side. The 200 cm^{-1} broad fs pump laser pulse would prepare a coherent superposition of all these levels. The TRPES data suggests that an apparent splitting of 11 cm^{-1} would be present in the upper group. For details, see the text.

the fs pump pulse had a broad bandwidth (200 cm^{-1}) which would coherently populate all of the state levels shown on the left side of Fig. 5, leading to wavepacket dynamics containing both an apparent exponential decay and an oscillatory component of, for example, 11 cm^{-1} . This proposal is discussed in further detail below.

We now consider the topography of the excited state potential surfaces. The S_2 state, while degenerate at D_{3h} geometries, undergoes Jahn–Teller distortion thereby lifting the degeneracy and leading to a set of C_{2v} minima on one of the degenerate components separated by a set of C_{2v} symmetry saddle points. Thus, in the diabatic picture, there will be two sets of conical intersections: (i) those between S_1 and the lower Jahn–Teller sheet (denoted $S_{2,x}$); and (ii) those corresponding to crossing between S_1 and the upper Jahn–Teller sheet (denoted $S_{2,y}$), where the labels x and y refer to orthogonal components of a doubly degenerate e' irreducible representation. Since the upper and lower JT sheets transform as a_1 and b_2 , respectively, in C_{2v} symmetry, it is clear on the basis of symmetry that the branching space (defined by the \mathbf{g} and \mathbf{h} vectors)^{2,52} of these two classes of intersections will be different. We expect, therefore, that there will be a differential nonadiabatic coupling along the x - and y -directions.

The branching space directions for the three sets of intersections of concern here are presented in Fig. 6. These are: on the left, the Jahn–Teller MECI; in the middle the C_s -constrained S_1 – $S_{2,x}$ MECI; on the right the C_s -constrained S_1 – $S_{2,y}$ MECI. It is important to note that for both the S_1 – $S_{2,x}$ and S_1 – $S_{2,y}$ intersections, the approach to the electronic degeneracy, given by the \mathbf{g} direction, is the same: the symmetric N-umbrella mode. By contrast, the \mathbf{h} directions are different for S_1 – $S_{2,x}$ and S_1 – $S_{2,y}$. This is necessarily so, given the symmetry of the electronic states involved and, in fact, the two \mathbf{h} directions transform as components of an e' coordinate comprised predominantly by θ_{CNC} angle bends and r_{CN} stretches. We expect that the difference between h_x and h_y is the origin of the differential nonadiabatic couplings along the x - and y -directions.

While these directions are defined nascently as linear combinations of valence internal coordinates, a total energy decomposition of the normal modes will identify those vibrations with significant overlap with the branching space coordinates. Employing the S_1 vibrational modes in Table S1† as a basis for nuclear motion, the \mathbf{g}

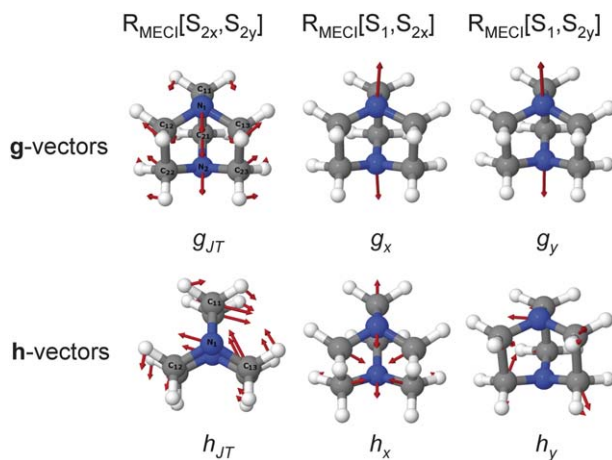


Fig. 6 Branching space directions determined at the minimum energy Jahn–Teller (left) and C_s -symmetry constrained $[S_1, S_2]$ conical intersections (middle and right). For the latter, note that g_x and g_y are the same: the symmetric umbrella mode. Conversely, the \mathbf{h} -directions are different, where h_x and h_y are components of an e' coordinate. This difference suggests that the nonadiabatic coupling should be different along the x and y directions. For details, see the text.

direction for both classes of intersection is comprised of approximately equal parts (35%) of modes ω_6 and ω_{17} , which correspond to the two, largely uncoupled, N-umbrella modes, and a secondary contribution (20%) from a CH wag mode, ω_3 . The \mathbf{h} directions for the S_1-S_{2x} and S_1-S_{2y} intersections have non-negligible overlap with each of the e' vibrational modes, where the largest contributions are from ω_{24} (25%, degenerate CN stretch) and ω_{26} (24%, degenerate CC stretch).

In Fig. 7 we show the potential curves for \tilde{S}_1 (red) and for \tilde{S}_2 along the x (blue) and y (green) directions. Due to JT distortion, the blue and green potentials are not identical. We calculated the energies of the $\tilde{S}_1-\tilde{S}_{2x}$ and $\tilde{S}_1-\tilde{S}_{2y}$ intersections, emphasised by black circles, and have confirmed that they are indeed different, with the $\tilde{S}_1-\tilde{S}_{2x}$ MECI being lower by approximately 1170 cm^{-1} . The $v=0$ eigenstates of the \tilde{S}_{2x} and \tilde{S}_{2y} potentials are nearly degenerate and are shown as the blue and green lines, respectively. These are located energetically above both MECIs. The energy of nearby vibrationally excited e' modes on the \tilde{S}_1 potential are shown as the red line, $\tilde{S}_1(v'[e'])$. Being doubly degenerate, its energy is the same along the x and y directions. Based on this picture, we are able to suggest an energy level scheme which is consistent with the experimental TRPES data.

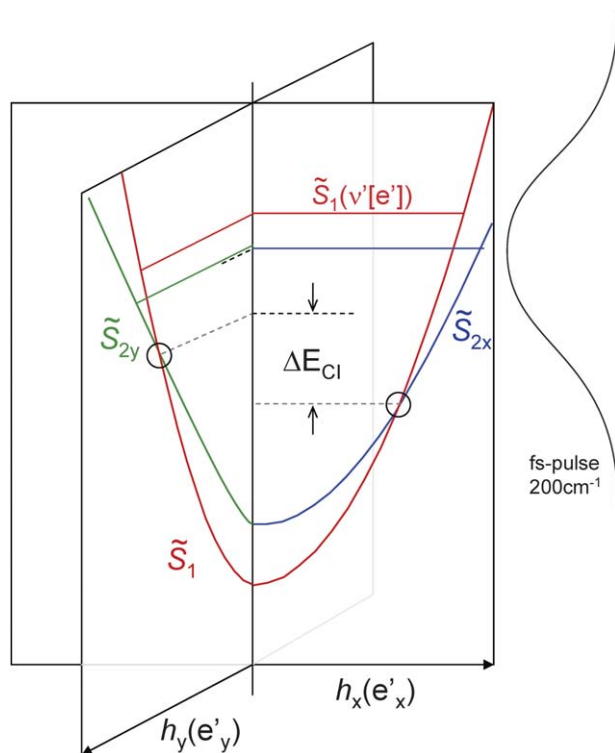


Fig. 7 Diabatic potential energy curves and zeroth-order (uncoupled) energy levels. The subscripts x and y refer to the orthogonal components of an e' doubly degenerate mode (in D_{3h} point group symmetry). The Jahn–Teller (JT) interaction lifts the S_2 electronic state degeneracy, yielding two JT sheets S_{2x} (blue) and S_{2y} (green) having different curvatures. The non-degenerate S_1 state (red) is symmetric along the x and y directions and will therefore intersect differently along these two directions. Our calculations reveal that there is a pair of non-degenerate S_2-S_1 MECIs, indicated by black circles. This asymmetry would lead to differential nonadiabatic coupling. The zero point energy of the nominal, nearly degenerate S_{2x} and S_{2y} curves are shown as green and blue lines, and are above both MECIs. The energy of a nearby vibrationally excited degenerate (e') S_1 level is shown as the red line. For details, see the text.

In Fig. 8 we show a coupling scheme between the \tilde{S}_2 and \tilde{S}_1 states which includes the differential nonadiabatic coupling of the two Jahn–Teller components \tilde{S}_{2x} and \tilde{S}_{2y} , with doubly degenerate, vibrationally excited $\tilde{S}_1(v'[e'])$ levels. The differential coupling leads to the pseudo three level system shown here (middle). Due to the high vibrational state density on the \tilde{S}_1 potential at the energy of the \tilde{S}_2 origin, there will actually be a dense set of $\tilde{S}_1(v'[e'])$ levels (red), shown on the right, which can couple with the nearly degenerate vibrationless $\tilde{S}_{2x}\tilde{S}_{2y}$ level (blue, green), shown on the left. In order to be consistent with both the \tilde{S}_2 absorption spectrum and the TRPES data, the nonadiabatic coupling must induce a splitting which is greater than 30 cm^{-1} but less than approximately 200 cm^{-1} . The lower component of this splitting is predominantly of \tilde{S}_2 character, indicated by the blue and green segments, with the minor \tilde{S}_1 character indicated by the red segments. The near x – y degeneracy of this level is apparently only minimally affected by the nonadiabatic coupling. In our scheme, this level would correspond to the 2.6 cm^{-1} wide origin peak reported in the \tilde{S}_2 absorption spectrum and is depicted on the lower left hand side of Fig. 5. It would undergo an apparent exponential decay, since it is actually composed of a dense set of irregularly spaced exact molecular eigenstates (black lines). For the upper component, the x – y degeneracy would be lifted by the differential nonadiabatic interaction discussed above and suggested by Fig. 7. This would lead to the two pseudo levels shown. We expect that these would be predominantly of \tilde{S}_1 character, as indicated by the red segment. Due to the differential interaction, they would be split, in this picture, by 11 cm^{-1} . The lower pseudo level would be the x component (blue), the higher level the y component (green). Due to the differential interaction, the \tilde{S}_{2x} contribution, shown by the blue segment, and the \tilde{S}_{2y} contribution, shown by the green segment, would not be equal. Again, these two pseudo levels would actually be composed of a high density of exact molecular eigenstates (black lines). Nevertheless, their envelope would be modulated so as to produce an apparent $\sim 11\text{ cm}^{-1}$ splitting. This notion is shown on the upper left hand side of Fig. 5.

The broad 200 cm^{-1} bandwidth of the 251 nm pump pulse coherently populates all the levels shown on the left side of Fig. 5. This wavepacket will evolve according to its level spacings. Due to the pseudo three level structure, we might expect three

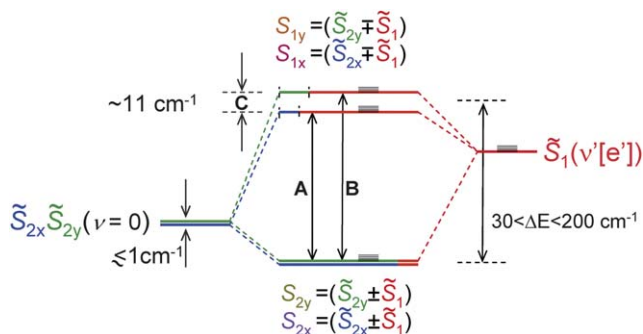


Fig. 8 A coupled pseudo three level system generated from the \tilde{S}_2 (blue and green) and \tilde{S}_1 (red) zeroth-order eigenstates. The components of \tilde{S}_2 couple differentially to the \tilde{S}_1 manifold, yielding a narrow, lower energy group $S_{2x}S_{2y}$ (predominantly blue and green) and a degeneracy-lifted S_{1x} (blue and red) and S_{1y} group (green and red), the individual levels of which are comprised of differing degrees of \tilde{S}_2 character. The femtosecond laser pulse creates a complex wavepacket in this pseudo 3-level system. The coherences **A**, between $S_{2x}S_{2y}$ and S_{1x} , and **B**, between $S_{2x}S_{2y}$ and S_{1y} , are understood as vibronic wavepackets oscillating between \tilde{S}_2 and \tilde{S}_1 zeroth-order electronic character. Due to their small energy difference **C**, the net electronic character of the full superposition state will be modulated at a low frequency (11 cm^{-1}), leading to a slow oscillation of the relative intensities of the \tilde{S}_2 and \tilde{S}_1 photoelectron bands during their apparent decay. For details, see the text.

nominal modulation frequencies to appear in the wavepacket signal. Referring to the middle (*i.e.* coupled) section of Fig. 8, these modulations would be due to the energy spacings between: (A) the lower (near degenerate) $\tilde{S}_{2x}\tilde{S}_{2y} \pm \tilde{S}_1$ level and the upper \tilde{S}_{1x} level (blue, red); (B) the same $\tilde{S}_{2x}\tilde{S}_{2y} \pm \tilde{S}_1$ level and the upper \tilde{S}_{1y} level (green, red); and finally (C) the upper \tilde{S}_{1x} level (blue, red) and the upper \tilde{S}_{1y} level (green, red). The energy level spacings in (A) and (B) would produce high frequency modulations (*e.g.* up to 200 cm^{-1}) of the wavepacket signal whereas that in (C) would produce a nominal 11 cm^{-1} modulation of the wavepacket signal. Somewhat in contradiction with this picture, the wavepacket signals shown in Fig. 4b do not show much spectral power at the higher frequencies expected from level spacings (A) and (B). However, it is important to note that the finite step size of the pump–probe time delay (N.B. this is unrelated to the pump or probe laser bandwidths) yields a limited sampling of the higher frequency wavepacket modulations, acting essentially as a frequency cut-off filter which reduces their spectral power. In this situation, the dominant wavepacket modulations would appear at the low frequency due to the level spacing (C). This picture is consistent with the slow modulations seen in the TRPES data. The overall apparent exponential decay of the zeroth-order S_2 state would be due to the dense, irregular level structure making up each of the three pseudo levels of Fig. 8. In this case, the dephasing rate due to this dense level structure seems to be on the same time scale as the 11 cm^{-1} oscillation due to level spacing (C), leading to the oscillatory decay seen in Fig. 3b.

What vibrational motions at conical intersections are associated with the wavepacket dynamics discussed above? The coherent superposition (A) would produce a vibrational motion along the x component of a nominal e' mode and a high frequency oscillation of the S_2/S_1 electronic character driven by this x motion. Likewise, the coherent superposition (B) would produce a vibrational motion along the y component of a nominal e' mode and a high frequency oscillation of the S_2/S_1 electronic character driven by this y motion. The fact that the oscillations along the x and y directions, given by the inverse level spacings (A) and (B), do not match means that there will be a slow (11 cm^{-1}) beating of the net S_2/S_1 electronic character at a frequency given by level spacing (C), consistent with experiment. The wavepacket motion corresponding to the coherent superposition state (C) can be understood with reference to the $[S_{2xy}, S_1]$ MECIs shown in Fig. 6. Motion along the \mathbf{g} directions preserve the zeroth-order Born–Oppenheimer character. Motion along the \mathbf{h} directions leads to a change in zeroth-order Born–Oppenheimer character. The directions g_x and g_y are the same: both bring the nitrogen p_z orbitals closer together *via* an umbrella-type motion. The wavepacket motion (C) that corresponds to oscillation of the zeroth-order Born–Oppenheimer electronic character will be comprised of components of e' modes that behave like a coherent superposition of the motions given by h_x and h_y . This vibration corresponds to small oscillations of the two N atoms in a plane parallel to the σ_h reflection plane, and concomitant small oscillations of the carbon atoms in planes at an angle with respect to the first one. This leads to a tilted angular oscillation of the nitrogen p_z orbitals along a shallow cone aligned with the three-fold symmetry axis. Due to the lack of rotational symmetry in the nonadiabatic coupling, this motion leads to a slow (11 cm^{-1}) oscillation in the electronic charge density distribution between the $3p_{xy}(+)$ and $3s(+)$ orbitals shown in Fig. 2. Corroboration of the picture of non-Born–Oppenheimer wavepacket dynamics in DABCO presented here must await more detailed *ab initio* computations.

5. Conclusions

The excited state dynamics of polyatomic molecules almost invariably involves well known failures of the adiabatic Born–Oppenheimer approximation. In particular, when conical intersections are of import there is typically a pronounced coordinate dependence to the nonadiabatic coupling, where passage through these regions of

strong coupling is characterised by ultrafast internal conversion of electronic to vibrational energy. The combination of high state densities with strong coordinate-dependent coupling presents a challenge to typical eigenstate-resolved spectroscopies. The time domain approach, through coherent superposition, permits the preparation of zeroth-order (*e.g.* Born–Oppenheimer) states and the interrogation of their subsequent dynamics. Making analogies with transition state dynamics on ground state surfaces, we are particularly interested in the development of heuristic approaches, similar to the Polanyi rules, for understanding the role of conical intersection topography and the efficacy of specific vibrational dynamics.

By analogy with the stationary phase evaluation of Franck–Condon integrals in order to determine their coordinate dependence, we can also, in principle, determine volumes in configuration space over which the nonadiabatic coupling integrals are large. These volumes are typically localised about conical intersections but can be nevertheless quite extended. An extended conical intersection volume and the extreme rapidity of these processes can combine to obscure the observation of specific vibrational motions at intersections. In this case, one relies fully on theory in order to determine the nonadiabatic dynamics. Here we have chosen to study conical intersections among Rydberg states of the high symmetry molecule DABCO, anticipating that the generally weak coupling between Rydberg states and the sparsity of non-zero coupling matrix elements will restrict conical intersection volumes, permitting direct observation of vibrational motions at such intersections. Indeed, we have directly observed *via* time-resolved photoelectron spectroscopy (TRPES) the modulation of zeroth-order electronic population by vibrational motions in DABCO. By combining with high level *ab initio* theory, we have developed a model for these dynamics which is consistent with the experimental results. Further evaluation of this model will, however, require high level structural and dynamics calculations. We anticipate that the combination of TRPES with quantum dynamics methods such as *ab initio* full multiple spawning⁵³ will lead to new and intuitive models for the study of electronically nonadiabatic processes in polyatomic molecules.

References

- 1 G. J. Atchity, S. S. Xantheas and K. Ruedenberg, *J. Chem. Phys.*, 1991, **95**, 1862–1876.
- 2 D. R. Yarkony, *Acc. Chem. Res.*, 1998, **31**, 511–518.
- 3 O. Schalk, A. E. Boguslavskiy and A. Stolow, *J. Phys. Chem. A*, 2010, **114**, 4058–4064.
- 4 O. Schalk, A. E. Boguslavskiy, M. S. Schuurman and A. Stolow, *J. Am. Chem. Soc.*, 2011, submitted.
- 5 G. Wu, A. E. Boguslavskiy, O. Schalk, M. S. Schuurman and A. Stolow, *J. Phys. Chem.*, submitted.
- 6 A. M. D. Lee, J. D. Coe, S. Ullrich, M. L. Ho, S. J. Lee, B. M. Cheng, M. Z. Zgierski, I. C. Chen, T. J. Martinez and A. Stolow, *J. Phys. Chem. A*, 2007, **111**, 11948–11960.
- 7 H. L. Tao, B. G. Levine and T. J. Martinez, *J. Phys. Chem. A*, 2009, **113**, 13656–13662.
- 8 A. M. Halpern, J. L. Roebber and K. Weiss, *J. Chem. Phys.*, 1968, **49**, 1348.
- 9 A. M. Halpern, *Chem. Phys. Lett.*, 1970, **6**, 296–298.
- 10 Y. Hamada, A. Y. Hirakawa and M. Tsuboi, *J. Mol. Spectrosc.*, 1973, **47**, 440–456.
- 11 D. H. Parker and P. Avouris, *J. Chem. Phys.*, 1979, **71**, 1241–1246.
- 12 R. W. Alder, R. J. Arrowsmith, A. Casson, R. B. Sessions, E. Heilbronner, B. Kovac, H. Huber and M. Taagepera, *J. Am. Chem. Soc.*, 1981, **103**, 6137–6142.
- 13 P. Avouris and A. R. Rossi, *J. Phys. Chem.*, 1981, **85**, 2340–2344.
- 14 V. Galasso, *Chem. Phys.*, 1997, **215**, 183–190.
- 15 C. T. Lin, C. J. Mertz and W. R. Mason, *J. Phys. Chem.*, 1989, **93**, 3514–3518.
- 16 M. A. Smith, J. W. Hager and S. C. Wallace, *J. Phys. Chem.*, 1984, **88**, 2250–2255.
- 17 S. T. Pratt, *Chem. Phys. Lett.*, 2002, **360**, 406–413.
- 18 G. J. Fisanick, T. S. Eichelberger, M. B. Robin and N. A. Kuebler, *J. Phys. Chem.*, 1983, **87**, 2240–2246.
- 19 M. Fujii, Y. Tsuchiya and M. Ito, *J. Phys. Chem.*, 1988, **92**, 2398–2400.
- 20 M. J. Watkins and M. C. R. Cockett, *J. Chem. Phys.*, 2000, **113**, 10560–10571.
- 21 A. Yokozeki and K. Kuchitsu, *Bull. Chem. Soc. Jpn.*, 1971, **44**, 72.

-
- 22 N. Gonohe, N. Yatsuda, N. Mikami and M. Ito, *Bull. Chem. Soc. Jpn.*, 1982, **55**, 2796–2802.
- 23 M. A. Quesada, Z. W. Wang and D. H. Parker, *J. Phys. Chem.*, 1986, **90**, 219–222.
- 24 D. Consalvo, M. Drabbels, G. Berden, W. L. Meerts, D. H. Parker and J. Reuss, *Chem. Phys.*, 1993, **174**, 267–276.
- 25 A. Staib, W. Domcke and A. L. Sobolewski, *Z. Phys. D, At., Mol. Clusters*, 1990, **16**, 49–60.
- 26 A. Stolow and J. G. Underwood, *Adv. Chem. Phys.*, 2008, **139**, 497–583.
- 27 A. Stolow, A. E. Bragg and D. M. Neumark, *Chem. Rev.*, 2004, **104**, 1719–1757.
- 28 C. C. Hayden and A. Stolow, *Photoionization and Photodetachment*, World Scientific, Singapore, 1999, vol. 10A.
- 29 L. Poisson, R. Maksimenska, B. Soep, J. M. Mestdagh, D. H. Parker, M. Nsangou and M. Hochlaf, *J. Phys. Chem. A*, 2010, **114**, 3313–3319.
- 30 T. S. Rose, M. J. Rosker and A. H. Zewail, *J. Chem. Phys.*, 1988, **88**, 6672–6673.
- 31 T. S. Rose, M. J. Rosker and A. H. Zewail, *J. Chem. Phys.*, 1989, **91**, 7415–7436.
- 32 V. Engel, H. Metiu, R. Almeida, R. A. Marcus and A. H. Zewail, *Chem. Phys. Lett.*, 1988, **152**, 1–7.
- 33 M. J. J. Vrakking, D. M. Villeneuve and A. Stolow, *J. Chem. Phys.*, 1996, **105**, 5647–5650.
- 34 M. Shapiro, M. J. J. Vrakking and A. Stolow, *J. Chem. Phys.*, 1999, **110**, 2465–2473.
- 35 B. Zhang, N. Gador and T. Hansson, *Phys. Rev. Lett.*, 2003, **91**, 173006.
- 36 P. Kruit and F. H. Read, *J. Phys. E: Sci. Instrum.*, 1983, **16**, 313–324.
- 37 S. Lochbrunner, J. J. Larsen, J. P. Shaffer, M. Schmitt, T. Schultz, J. G. Underwood and A. Stolow, *J. Electron Spectrosc. Relat. Phenom.*, 2000, **112**, 183–198.
- 38 T. H. Dunning, *J. Chem. Phys.*, 1970, **53**, 2823.
- 39 T. H. D. Jr. and P. J. Hay, in *Methods of Electronic Structure Theory*, vol. 2, ed. H. F. S. III, Plenum Press, 1977.
- 40 D. Feller, *J. Comput. Chem.*, 1996, **17**, 1571–1586.
- 41 K. L. Schuchardt, B. T. Didier, T. Elsethagen, L. S. Sun, V. Gurumoorthi, J. Chase, J. Li and T. L. Windus, *J. Chem. Inf. Model.*, 2007, **47**, 1045–1052.
- 42 D. R. Yarkony, *J. Phys. Chem. A*, 2004, **108**, 3200–3205.
- 43 R. Shepard, *Int. J. Quantum Chem.*, 1987, **31**, 33–44.
- 44 H. Lischka, M. Dallos and R. Shepard, *Mol. Phys.*, 2002, **100**, 1647–1658.
- 45 H. Lischka, M. Dallos, P. G. Szalay, D. R. Yarkony and R. Shepard, *J. Chem. Phys.*, 2004, **120**, 7322–7329.
- 46 M. Dallos, H. Lischka, R. Shepard, D. R. Yarkony and P. G. Szalay, *J. Chem. Phys.*, 2004, **120**, 7330–7339.
- 47 H. Lischka, R. Shepard, F. B. Brown and I. Shavitt, *Int. J. Quantum Chem.*, 1981, 91–100.
- 48 H. Lischka, R. Shepard, R. M. Pitzer, I. Shavitt, M. Dallos, T. Muller, P. G. Szalay, M. Seth, G. S. Kedziora, S. Yabushita and Z. Y. Zhang, *Phys. Chem. Chem. Phys.*, 2001, **3**, 664–673.
- 49 R. G. Gordon, *J. Chem. Phys.*, 1966, **44**, 1830–1836.
- 50 J. S. Baskin, M. Chachisvilis, M. Gupta and A. H. Zewail, *J. Phys. Chem. A*, 1998, **102**, 4158–4171.
- 51 O. Schalk and A. N. Unterreiner, *Phys. Chem. Chem. Phys.*, 2010, **12**, 655–666.
- 52 D. R. Yarkony, in *Conical Intersections: Electronic Structure, Dynamics and Spectroscopy*, ed. H. K. W. Domcke, D. R. Yarkony, World Scientific, 2004.
- 53 M. Ben-Nun and T. J. Martinez, *Adv. Chem. Phys.*, 2002, **121**, 439–512.